ACS APPLIED MATERIALS & INTERFACES

www.acsami.org

Research Article

Revealing the Modulation Effects on the Electronic Band Structures and Exciton Properties by Stacking Graphene/h-BN/MoS_2 Schottky Heterostructures

Xudan Zhu, Junbo He, Weiming Liu, Yuxiang Zheng, Chuanxiang Sheng, Yi Luo, Shaojuan Li,* Rongjun Zhang,* and Junhao Chu

Cite This: *ACS Appl. Mater. Interfaces* 2023, 15, 2468−2478

Read Online

ABSTRACT: Stacking two dimensional tunneling heterostructures has always been an important strategy to improve the optoelectronic device performance. However, there are still many disputes about the blocking ability of monolayer (1L-) h-BN on the interlayer coupling. Graphene/h-BN/MoS_2 optoelectronic devices have been reported for superior device results. In this study, starting with graphene/h-BN/MoS_2 heterostructures, we report experimental evidence of 1L-h-BN barrier layer modulation effects about the electronic band structures and exciton properties. We find that 1L-h-BN insertion only partially blocks the interlayer carrier transfer. In the meantime, the 1L-h-BN barrier layer weakens the interlayer coupling effect, by decreasing the efficient dielectric screening and releasing the quantum confinement. Consequently, the optical conductivity and plasmon excitation slightly improve, and the electronic band structures remain unchanged in graphene/h-BN/MoS_2, explaining their fascinating optoelectronic responses. Moreover, the excitonic binding energies of graphene/h-BN/MoS_2 redshift with respect to the graphene/MoS_2 counterparts. Our results, as well as the broadband optical constants, will help better understand the h-BN barrier layers, facilitating the developing progress of h-BN-based tunneling optoelectronic devices.

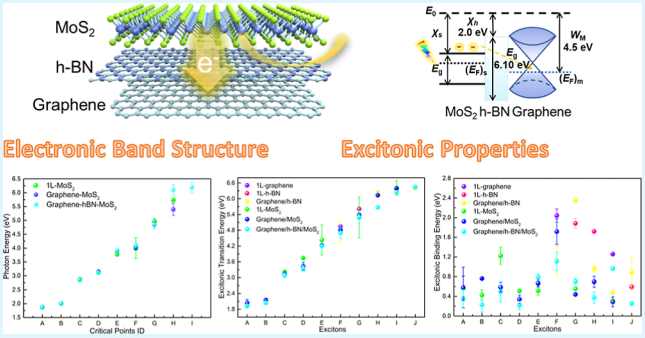

KEYWORDS: *graphene/h-BN/MoS_2 heterostructures, tunneling effect, interlayer coupling, electronic band structures, excitons*

1. INTRODUCTION

The two-dimensional (2D) heterostructures have presented intriguing and abundant new phenomenon, induced by interface quantum coupling. Variety of nano-optoelectronic devices have been reported, utilizing the interface-induced novel effects in 2D heterostructures.[1,2] The ability to engineer the electronic band structures and exciton states is of great importance to these applications. For the past decades, several methods tuning a 2D heterostructure's electronic band gap and excitonic properties have been discovered, such as, heterostructure framework design, substrate effect, electrostatic grating, background doping, and mechanical strain.[3,4] Among them, inserting insulating layers is an effective strategy without significantly introducing fabrication complexities. Since hexagonal boron nitride (h-BN) has intriguing properties including no hanging bonds or charged impurity atomic flatness, uniform and effective dielectric screening of the surrounding charged impurities, and self-cleaning effect at the heterointerface, hence, h-BN usually serves as tunnel barrier layers in 2D heterostructures.[5−7] However, there still exist more exploration room to develop the experimental study on monolayer (1L-) h-BN barrier layers' modulation effects on the interlayer coupling and evaluation of its blocking strength on the interlayer charge transfer.

Recently, graphene/MoS_2 heterostructures have attracted substantial attention from the fields of material science, condensed matter physics, and optoelectronic applications, including ultrahigh gain photodetectors,[8−12] high speed communications,[13] high energy conversion efficiency solar cells,[14] high sensitivity chemical and biological sensors,[15] and so forth.[16,17] This is mostly derived from the fact that graphene can assemble with MoS_2 into perfect Schottky heterostructures with tunable barrier height.[17−19] Especially, the graphene/MoS_2 photodetectors can work in a self-powered mode, exhibiting excellent responsivity, fast photoresponse rate, low dark current, and large on/off ratio without external power supply.[20] Thus, taking graphene/MoS_2 heterostructure as a

Received: November 8, 2022
Accepted: December 21, 2022
Published: December 30, 2022

https://doi.org/10.1021/acsami.2c20100
ACS Appl. Mater. Interfaces 2023, 15, 2468−2478

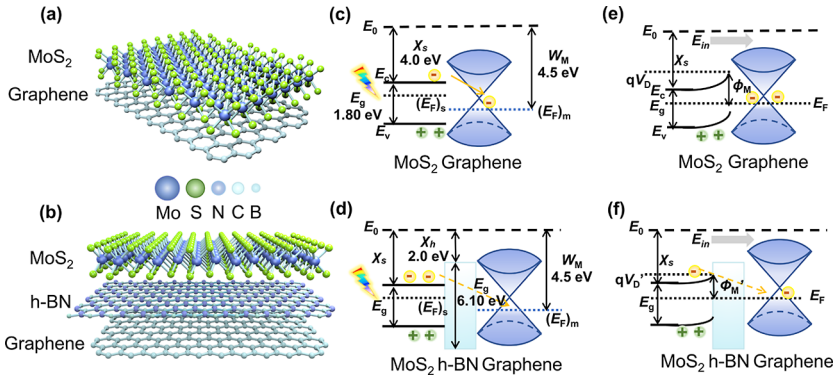

Figure 1. (a,b) Schematic illustration of the graphene/MoS_2 and graphene/h-BN/MoS_2 heterostructures. Schematic band diagrams at the flat band model (c,d) and the equilibrium states (e,f) of the heterostructures [E_0, the vacuum level; E_c, conduction band minimum; E_v, valence band maximum; E_g, band gap; $(E_F)_{s/m}$, individual Femi levels of MoS_2 and graphene; E_F, the Femi level at equilibrium states; $\chi_{s/h}$, electron affinity of MoS_2/h-BN; W_M, work function of graphene; ϕ_M, electron Schottky barrier height between graphene and MoS_2; $\phi_{M'}$, ϕ_M after 1L-h-BN insertion; E_{in}, build-in electric field caused by the space charge region].

platform, exploring the 1L-h-BN barrier layer modulation effects on interlayer coupling and interlayer charge transfer is the object of this work. Furthermore, we aim to experimentally reveal the 1L-h-BN insertion effects on the electronic band structures and exciton properties.

The properties and applications of graphene/h-BN/MoS_2 heterostructures are currently the subject of a very active research field.[9,21−30] However, there are still many disputes about the best h-BN thickness chosen for optoelectronic applications. By monitoring the I−V behavior of the graphene/h-BN/MoS_2 trilayer photodetector, Li et al.[9] reported that the photovoltaic effect can be substantially recovered by 1L-h-BN insertion. The interlayer transport of electrons can be considerably hindered by the 1L-h-BN barrier. This conclusion is consistent with some other studies, which, in common, affirmed the enough blocking ability of 1L- (or 2L-) h-BN.[21−25] Focusing on the same issue, by studying the detectivity of the photodetector with the tunneling structure, in 2016 Vu et al.[26] reported that when the thickness of h-BN has been optimized to 7 nm, the dark current was minimized while the high tunneling current was maintained. This result was supported by other experimental studies that the best h-BN thickness is around 3−7 nm. Because it can be a creative trade-off between the optimal tunneling barrier and the high photoresponsivity.[27−29] However, Jeong et al.[30] gained approximately 10 times higher current for the tunneling diode compared with p−n diode without h-BN, where the barrier layer thickness approached 20 nm. Then, we can see that although h-BN is widely used for stacking tunneling van der Waals heterostructures, the optimal thickness of the h-BN barrier layer remains unclear. Considering the trends in the construction of whole two-dimensional monolayer thin-film devices, we focused on exploiting the blocking ability of 1L-h-BN on the interlayer coupling effects and interlayer charge transfer.

In this study, by using spectroscopic ellipsometry (SE),[31,32] we reported broadband (ranging from 200−1000 nm) optical properties of graphene/MoS_2 and graphene/h-BN/MoS_2 heterostructures, including dielectric functions ($\varepsilon = \varepsilon_1 + i\varepsilon_2$), complex optical conductivity ($\sigma^F = \sigma^F{}_1 + \sigma^F{}_2$), energy loss functions [$\mathrm{Im}(\varepsilon^{-1})$], absorption coefficients (α), critical points (CPs), and excitons (transition energies and binding energies). The systemically experimental study of the broadband optical properties is also important prerequisites toward its widely popularization and application toward photoelectronic devices. Especially, in the SE data analysis process, we first used the point-by-point mathematical inversion and then experimentally checked the fitting results, which can be extended to the study of optical properties of other 2D material membrane systems. Noting that CPs (i.e., Van Hove Singularities) are corresponding to significant direct interband transitions over Brillouin Zone (BZ).[33] By monitoring the CP transition energy evolution between two heterostructures, the 1L-h-BN insertion regulating effect on electronic band structures was experimentally unveiled. Our work offered comprehensive experimental evidence of the true blocking effect of adding the 1L-h-BN barrier layer into the graphene/MoS_2 heterointerface by reliable and high-sensitive experimental methods: Raman spectra, photoluminescence (PL) spectra, and SE method. Furthermore, dielectric screening effect and quantum confinement effect induced by 1L-h-BN insertion were also taken into consideration among analysis of the physical mechanism of optical property regulation. Our results, as well as the reported broadband optical constants, will help better understand the h-BN barrier layer modulation effects, facilitating the developing progress of h-BN based tunneling optoelectronic devices.

2. RESULTS AND DISCUSSION

The 1L-graphene, 1L-h-BN, and 1L-MoS_2 were synthesized using the chemical vapor deposition (CVD) method. Bilayer (graphene/h-BN and graphene/MoS_2) and three-layer (graphene/h-BN/MoS_2) heterostructures were stacked using the poly(methyl methacrylate) (PMMA) carrying layer wet-transfer method. Each transfer operation was followed by the annealing process once. All the films were 1 × 1 cm in size and all transferred onto *c*-plane (0001) sapphire substrates for subsequent surface topography characterization and optical spectroscopy tests.

Figure 1a,b shows the schematic illustration of the graphene/MoS_2 and graphene/h-BN/MoS_2 heterostructures, where upper layers successively completely covered the bottom layers. Referred to the previous reported electron affinity (χ) of MoS_2 (χ_s = 4.0 eV) and h-BN (χ_h = 2.0 eV),[26] as well as the work function (W_M = 4.5 eV) of graphene,[9] the schematic band diagrams at the flat band model (Figure 1c,d) and the equilibrium states (Figure 1e,f) of graphene/MoS_2 and graphene/h-BN/MoS_2 heterostructures are depicted, respectively. In our work, the transferred CVD 1L-graphene film is

https://doi.org/10.1021/acsami.2c20100
ACS Appl. Mater. Interfaces 2023, 15, 2468−2478

slightly p-doped, which is verified by the Raman spectra in the next section. Note that the graphene films synthesized by CVD is p-doped by the transfer process, moisture/oxygen adsorption, or substrate impurities, which has been found in numbers of research studies before.[10] Because there is no hanging bonds or surface states in the heterointerfaces, hence the graphene/MoS_2 can be described as an ideal metal–semiconductor contact Schottky barrier model.[17] The optical microscopy images of the transferred heterostructure samples are shown in Supporting Information (Figure S1a–c). The atomic force microscopy (AFM) was implemented to examine the uniformity and surface roughness (Figure S1d–h, Supporting Information). In the surface topography characterization section, we observed no evidence of impurities or wrinkles, indicating the uniformity and high quality of the transferred samples.

First, let us analyze the band alignment and interlayer coupling in graphene/MoS_2 heterostructures. For separate MoS_2 and graphene (Figure 1c), they share the same vacuum energy level E_0. Obviously, the Femi energy of MoS_2 $(E_F)_s$ is higher than that of graphene $(E_F)_m$. After stacking into graphene/MoS_2 heterostructures, strong interlayer coupling effect makes this structure a unified electronic system. Electrons transfer from the MoS_2 layer to the graphene layer, which results in the negatively charged graphene surface and the positively charged MoS_2 surface. This carrier distribution induced a build-in electric field E_{in}. Since the carrier concentration of MoS_2 is much lower than that of graphene, the positive charges are located in the relatively thick surface layer of MoS_2, with the consequence that the band bending happens in the MoS_2 layer. Then, when the system reached an equilibrium state (Figure 1e), the two materials have the same Femi level E_F. The build-in electric field points from MoS_2 interior to the surface, that is, forming surface barrier, which hinders the interlayer electron exchange. The height of the electron barrier on the MoS_2 side (qV_D) is described using eq 1

$$qV_D = (E_F)_s - (E_F)_m \tag{1}$$

The height of the electron barrier on the graphene side is described using eq 2

$$\phi_M = W_M - \chi_s \tag{2}$$

ϕ_M largely determines the peculiarity of Schottky barrier diodes.

Then, we move on to the graphene/h-BN/MoS_2 heterostructure. Owing to a large band gap of 1L-h-BN (6.1 eV in this work), 1L-h-BN becomes a barrier layer, blocking the interlayer coupling (Figure 1d). Additionally, 1L-hBN is known as an insulator; thus, it cannot exchange charges with the materials on both sides. As a result, 1L-hBN cannot be considered as surface states but more like a square barrier with electron barrier height $U_{0e} = \chi_s - \chi_h \sim 2.0$ eV and hole barrier height $U_{0h} = \chi_h + E_{gh} - E_{gs} - \chi_s \sim 2.3$ eV. Then, the carrier direct tunneling probability D can be evaluated using eq 3[34]

$$D = D_0 \exp\left(-\frac{2}{\hbar}\sqrt{2\mu(U_0 - E)d}\right) \tag{3}$$

D_0 is a constant; $\hbar$ is the reduced Planck constant; μ is the mass of carriers ($\mu_e \ll \mu_h$); E is the energy of carrier; and d is the effective thickness of the h-BN barrier, which is related to its dielectric constant. It is expected that when the system is at equilibrium as shown in Figure 1f, electrons in the conduction band of MoS_2 have a greater chance of tunneling through the h-BN barrier layer to the graphene layer compared to the holes in the MoS_2 valence band. In order to experimentally quantify the tunneling possibility of the electrons in MoS_2, that is, blocking ability of 1L-h-BN on the interlayer coupling effects in graphene/h-BN/MoS_2 heterostructures, we carried out following spectral research experiments.

2.1. Study of Interlayer Coupling by the Raman Spectra. The Raman spectra of the heterostructures and the corresponding component monolayer films are presented in Figure 2. The respective Raman spectra of the films are

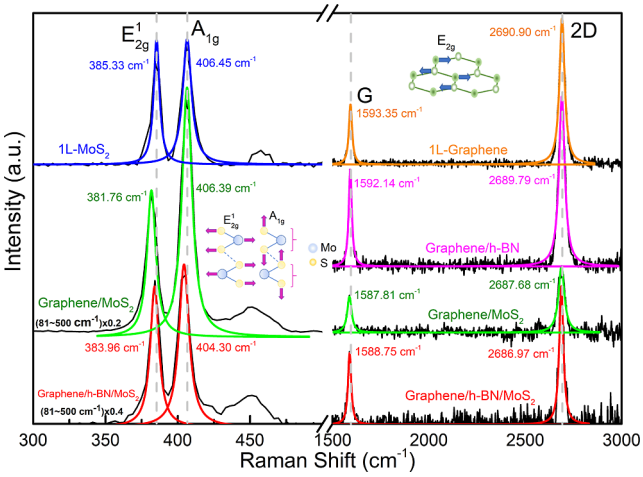

Figure 2. Raman spectra of 1L-MoS_2, 1L-graphene, graphene/h-BN, graphene/MoS_2, and graphene/h-BN/MoS_2 films. The insets depict the phonon modes responsible for the in-plane E_{2g}^1, out-of-plane A_{1g} of MoS_2, and E_{2g} (G peak) of graphene. For legibility of graphene vibration modes in the heterostructures, the Raman spectra within the 81–500 cm^{-1} range in graphene/MoS_2 and graphene/h-BN/MoS_2 films have been decreased by a factor of 0.4 and 0.2, respectively. The colorful multi-peaks were fitted by the Lorentzian function. Gray vertical dashed lines indicated the Raman shifts in 1L samples.

summarized in Supporting Information as Figure S2a–e. Moreover, all prominent peaks of the graphene layers in different samples were fitted with Lorentzian functions to extract the peak position, full width at half maximum (w), and intensity (I). The detailed fitting parameters are compared in Table S1 Supporting Information.

For the MoS_2 films, the two signature Raman peaks, the E_{2g}^1 and A_{1g} modes, were clearly observed (see Figure 2 left panel, and Figure S2b,d,e in the Supporting Information). The insets in Figure 2 depict the respective vibration modes of these two peaks, whose energy differences between these two modes in different samples claim that the MoS_2 layers are all monolayers.[35] Regarding the Raman spectra for monolayer graphene layers, two prominent peaks were obtained, the G (vibration mode depicted as E_{2g} inset of Figure 2 right panel) and 2D peaks. For the 1L-graphene sample, the two Raman modes were positioned at ~1593.35 and 2690.90 cm^{-1}, respectively, as well as their intensity ratio (I_{2D}/I_G = 2.43, Table S1 in Supporting Information), introducing its monolayer structure.[36] For the graphene/h-BN/MoS_2 sample, the 2D peak was described by a single Lorentzian function with w of 25.91 cm^{-1} (see Table S1 in Supporting Information), suggesting that the graphene layer was monolayer.[19] Especially, the D modes of graphene were not observed in all the samples (usually at ~1350 cm^{-1}), clarifying that there was no defects in

https://doi.org/10.1021/acsami.2c20100
ACS Appl. Mater. Interfaces 2023, 15, 2468–2478

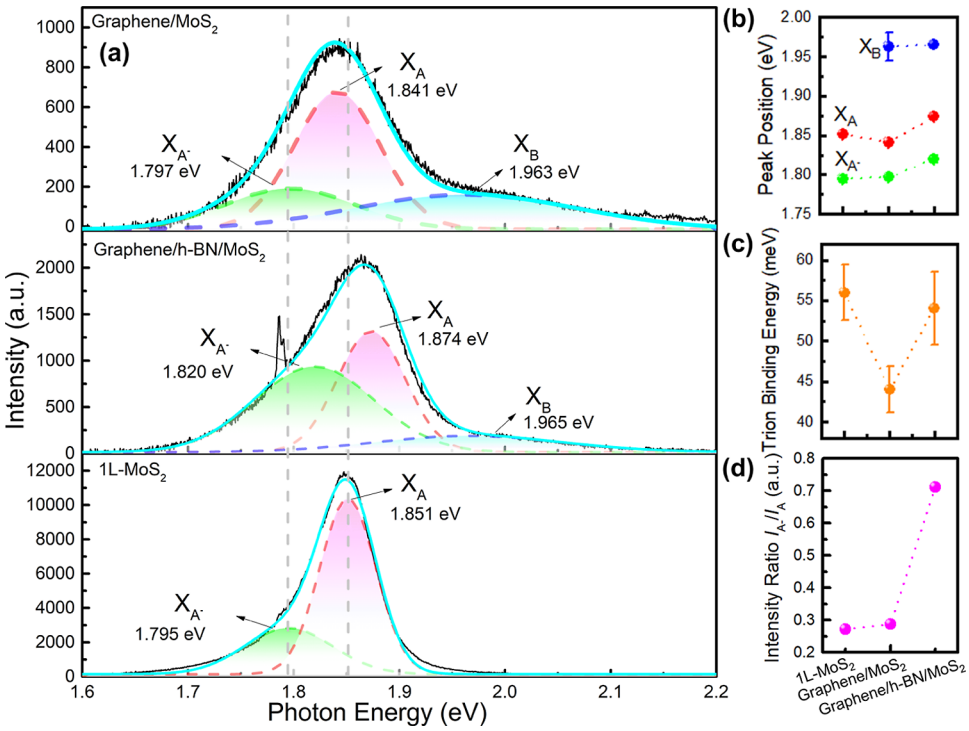

Figure 3. (a) PL spectra of the samples, where colorful dashed multi-peaks were obtained by Gaussian fitting. The vertical gray dashed lines indicated the PL positions of the trion (X_{A-}) and A exciton (X_A) of 1L-MoS_2. Comparison of (b) PL peak positions and (c) trion binding energies of the MoS_2 layers. (d) Intensity ratios of the X_{A-} and X_A of MoS_2 layers in different samples. The detailed information of the peaks is listed in Supporting Information Table S2.

transferred graphene layers.[37] It is noteworthy that in comparison with previous intrinsic graphene results[36] (Raman results of graphene at charge neutral point), the G and 2D peak blue shifted and I_{2D}/I_G decreased in this work, suggesting that the 1L-graphene was p-doped here, as well as in other heterostructures in this work. The G peak position (I_{2D}/I_G) blueshifts (decreases) monotonically by increasing the doping level of graphene ($|E_F - E_{Dirac}| > 0$), while the 2D peak position blueshifts when p-doped ($(E_{Dirac} - E_F) > 0$) and redshifts when n-doped ($(E_F - E_{Dirac}) > 0$).[19,36,38] This is consistent with the band alignment illustrations in Figure 1c−f. With respect to the 1L-h-BN E_{2g}^1 Raman mode, which was supposed at around 1363−1367 cm^{-1},[32,39,40] it become obscure in graphene/h-BN and graphene/h-BN/MoS_2 heterostructures. This can be attributed to its weak intensity, relatively high ambient noise signal, and reduced light transmittance of the top MoS_2 layer. The monolayer structure of h-BN in this work can be proved by the absorption edges in absorption coefficients (α) and transmittance functions in Supporting Information (Figure S6).

To investigate the interlayer coupling in heterostructures, we first monitored the Raman shift in the MoS_2 layers. Compared to the separate MoS_2 monolayer, the spectroscopic parameters for MoS_2 in graphene/MoS_2, E_{2g}^1 redshift and A_{1g} slightly redshift. The redshift of the E_{2g}^1mode can be attributed to the build-in strain (introduced by mismatch of the lattice constants) and increased efficient dielectric screening by the bottom graphene layer.[41,42] Referring to previous reports,[43,44] the efficient vertical dielectric constants of h-BN, graphene, and MoS_2 are ∼4.5, 9, and 6.3, respectively. On the other hand, the A_{1g} mode of MoS_2 is proved coupling stronger to electrons, thus sensitively to interlayer charge transfer. The A_{1g} slightly redshift in this work has also been observed in previous research studies,[18] although if only the charge transfer factor was considered, electrons transfer from MoS_2 to graphene would make MoS_2 less n-doped; consequently, the A_{1g} is expected to blueshift (as found in some studies[10,45]). Hence, besides charge transfer or efficient dielectric screening, other interlayer coupling effects or the adsorption of impurities may play a part in this process, which was not the research emphasis in this work. The Raman shifts suggested the strong interlayer coupling in graphene/MoS_2 heterostructures. Furthermore, in graphene/h-BN/MoS_2 heterostructures, the redshift of E_{2g}^1 reduced and redshift of A_{1g} increased, as results of largely released build-in strain and reduced dielectric screening by 1L-h-BN insertion, respectively. As expected, the 1L-h-BN can partly weaken the interlayer coupling. As revealed in previous work, due to the atomic flat surface of h-BN and the weak interlayer coupling effect in the MoS_2/h-BN heterointerface, the build-in strain is relatively small between h-BN and MoS_2.[46]

Next, we focused on the graphene Raman features (see Figure 2 right panel). Compared with isolated 1L-graphene, the positions of the G and 2D peaks for graphene in the graphene/MoS_2 redshift (located at 1592.14 and 2689.79 cm^{-1}) indicate that the graphene is less p-doped. Subsequently, the G peak blueshifts and 2D peak redshifts after 1L-h-BN insertion, declaring that the graphene layer was less p-doped. Additionally, in this context, the reduced dielectric screening effect induced by the 1L-h-BN barrier layer and improved thickness in the 2D system also came into play. Note that the 1L-h-BN layer did not exchange charge with the bottom graphene, as evidence that the graphene Raman features in graphene/h-BN are basically the same as those of the separate 1L-graphene. In the meantime, there is no interlayer charge

https://doi.org/10.1021/acsami.2c20100
ACS Appl. Mater. Interfaces 2023, 15, 2468−2478

transfer at the MoS_2/h-BN heterointerface, either.[47,48] These Raman findings demonstrated the strong interlayer coupling in graphene/MoS_2 heterostructures, which was somewhat attenuated by the 1L-h-BN insertion, especially the efficient dielectric screening effect and interlayer charge transfer.

2.2. Investigate the Interlayer Charge Transfer by the PL Spectra. For definite blocking strength of the 1L-h-BN barrier layer, PL spectroscopy was carried out. Figure 3a presents the PL spectra of different samples, where two significant PL peaks were observed in 1L-MoS_2, while three PL peaks were found in the heterostructures. Considering the high optical transparency of 1L-h-BN and relatively low optical absorption of 1L-graphene, these PL peaks were reasonably aligned to the trion (X_{A^-}), A exciton (X_A), and B exciton (X_B) of the MoS_2 layers. The X_B peak in 1L-MoS_2 were covered by high PL intensity of other two peaks. The PL intensity comparison and full range (1.35−2.32 eV) PL spectra of the samples are shown in Supporting Information (Figure S3), and the detailed multi-peak Gaussian fitting parameters are listed in Table S2 in Supporting Information.

It is evident that after being transferred onto top of graphene, the absolute PL intensity value of the MoS_2 layer decreased significantly (strong PL quenching), which clarified the efficient interlayer charge transfer and strong interlayer coupling effects in graphene/MoS_2. This strong PL quenching phenomenon has been reported in variety of previous research studies.[9,18,45] Furthermore, after combining with 1L-h-BN barrier layer, the PL quenching was reduced. The PL intensity of graphene/h-BN/MoS_2 was doubled versus that of graphene/MoS_2, but it is still an order of magnitude smaller than that of the 1L-MoS_2 film. This demonstrates that only a minor part of the interlayer charge transfer is blocked by 1L-h-BN intercalation. Nevertheless, the interlayer coupling between top MoS_2 and bottom graphene still existed, that is to say, these two components cannot be regarded as independent layers. This is the same as the results aforementioned in the Study of Interlayer Coupling by the Raman Spectra section. Besides, the dielectric screening effect of 1L-h-BN on charged impurities on the lower interface may also contributed to the enhanced PL intensity in graphene/h-BN/MoS_2,[5] which helps reduce the scattering to photogenerated carriers, improving the recombination efficiency, and enhancing the integral PL intensity.

Figure 3b−d plots the PL peak positions, trion binding energies (E_T), and intensity ratio (I_{A^-}/I_A) of the MoS_2 layers in different samples, respectively. According to previous research studies, an effective mass model is successful in predicting the binding energies of neutral excitons and trions. Hence, the intensity ratio of X_{A^-} and X_A can be derived as eq 4[18,49]

$$\frac{I_{A^-}}{I_A} = \frac{\gamma_{A^-}}{\gamma_A}\frac{\pi\hbar^2\mu_{A^-}}{4\mu_A m_e}\frac{n_e}{k_B T}\exp\left(\frac{E_T}{k_B T}\right) \tag{4}$$

where γ_{A^-} and γ_A are the radiative decay rates of X_{A^-} and X_A, μ_{A^-} and μ_A are the effective mass of X_{A^-} and X_A, m_e is the electron mass, n_e is the free electron concentration, T is the temperature, k_B is the Boltzmann constant, and E_T is the trion binding energies (PL peak energy differences between X_{A^-} and X_A). Thus, the trion spectral weight (I_{A^-}/I_A) is governed by the variation of n_e and E_T. Therein, E_T can be efficiently modulated by n_e,[49] strain, and dielectric screening.[3] It can be seen from Figure 3b−d that the peak positions and E_T red shifted in graphene/MoS_2. As expected, the MoS_2 is less n-doped since delivering electrons to graphene in graphene/MoS_2; as a consequence, n_e decreased, leading to reduced E_T. However, I_{A^-}/I_A rarely changed, which did not match the expectation. This could be caused by experimental errors or influence from impurities. During the process, besides the n_e modulating effect, strain and dielectric screening also played an important role. As revealed in Raman analysis, stacking graphene/MoS_2 leading to increased build-in strain and increased dielectric screening effect with respect to 1L-MoS_2, all these factors would redshift E_T and peak positions.

Subsequently, we focused on studying these effects induced by 1L-h-BN insertion on the PL signals. As revealed in Figure 3b−d, the X_A peak positions, E_T, and I_{A^-}/I_A significantly blue shifted in graphene/h-BN/MoS_2 heterostructures, compared with the values in graphene/MoS_2 heterostructures. This suggested that the build-in strain, efficient dielectric screening, and interlayer charge transfer were partly blocked by the 1L-h-BN barrier layer. Nonetheless, benefited from the dielectric screening effect of 1L-h-BN on charged impurities on the lower interface,[46,50−52] the trion spectral weight even enhanced over that of 1L-MoS_2, declaring the potential application prospect of the graphene/h-BN/MoS_2 heterostructure.

According to previous literature,[53] X_A and X_B are intralayer neutral excitons assigned to the splitting valence band at the high-symmetry K point in the BZ. Comparing the X_B peak in the graphene/MoS_2 and graphene/h-BN/MoS_2, assuming that the valence band splitting Δ_v (PL energy difference between X_A and X_B) remain stable during 1L-hBN insertion, the evolution trend of X_B will be the same as that of X_A. However, the X_B peak is nearly unchanged (as shown in Figure 3b), indicating the altering of Δ_v. Herein, we considered three possible factors introduced by 1-hBN insertion: the quantum confinement effect, build-in strain, and effective dielectric screening. First, the releasing quantum confinement effect in graphene/h-BN/MoS_2 will increase the Δ_v,[54,55] which cancels out the expected blueshift observed in X_A. Second, as reported by He et al.,[56] the spin−orbit interactions arise from the inner parts of the atoms and are insensitive to the strain-induced variation of the atomic bond lengths. Third, as revealed by Waldecker et al.,[43] the change of effective dielectric screening only leads to rigid shifts to the electronic bands. Thus, the Δ_v is independent to dielectric screening. By reason of the foregoing, the stable X_B peak in graphene/h-BN/MoS_2 is due to the increased Δ_v (caused by increased thickness), counteracting the blue shift of the neutral exciton PL peaks.

2.3. Photoconductivity and Energy Loss Function. Photoconductivity is an important constant describing the optical properties of the materials, which can be calculated from dielectric responses.[57] Herewith, we studied the broad-band optical properties of the samples by spectroscopic ellipsometry (SE), by which the refractive index (n) and extinction coefficient (k) of the samples can be extracted very accurately. Then, with n and k, other crucial optical parameters of the samples, such as dielectric functions ($\varepsilon_1 + i\varepsilon_2$), optical conductivity ($\sigma_1^F + i\sigma_2^F$), energy loss functions [$\mathrm{Im}(\varepsilon^{-1})$], and absorption coefficients (α), can be derived accordingly.[31,32,58] The detailed SE analysis and Kramers−Kronig consistency checking processes were introduced in the Supporting Information, from which we demonstrated that the point-by-point fitting results were checked by the consistency of the experimental parameters and generated SE data (Figure S4 in Supporting Information), PL and transmittance spectra measurement results. This suggested that during the SE data

https://doi.org/10.1021/acsami.2c20100
ACS Appl. Mater. Interfaces 2023, 15, 2468−2478

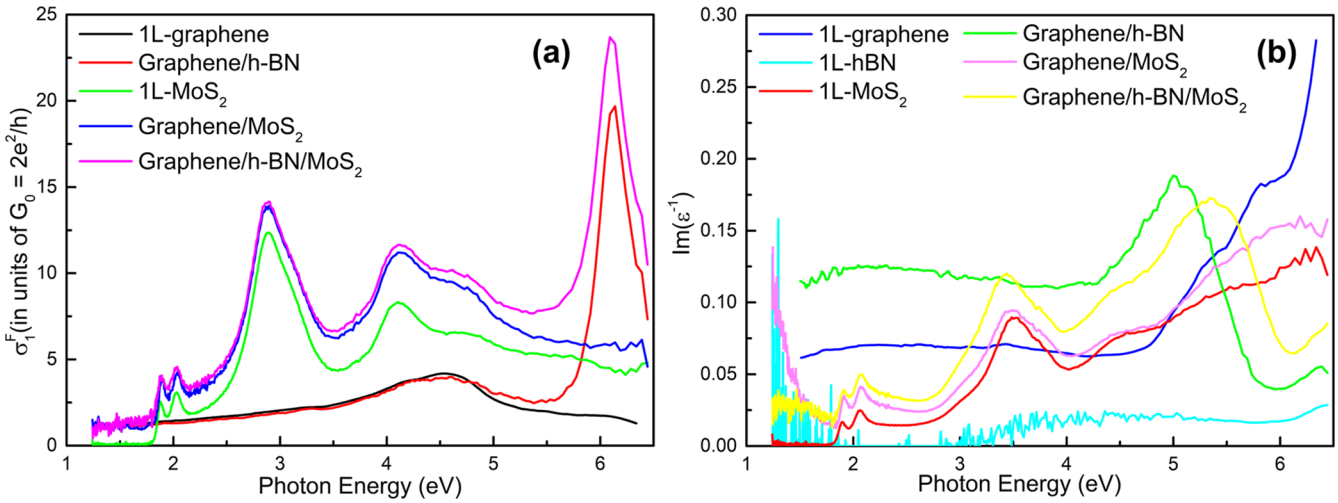

Figure 4. (a) Real part of optical conductivities (σ_1^F) in units of $G_0 = 2e^2/h$ and (b) energy loss functions [$\mathrm{Im}(\varepsilon^{-1})$] of the samples.

analysis process, the ellipsometric parameters can be first mathematical inverted using the point-by-point method and then experimentally checked by other experimental results. This method can be fruitfully exploited to obtain reliable optical information on other 2D systems.

We report the real part of the optical conductivities (σ_1^F) of the samples over a broadband range (1.2−6.5 eV), as shown in Figure 4a, which were calculated through the corresponding dielectric functions [the complex optical constants ($n + ik$) were plotted, as shown in Supporting Information Figure S5, equivalent to dielectric functions] using eqs 5 and 6[32,59]

$$\sigma(E) = \sigma_1(E) + i\sigma_2(E) = -i\frac{\varepsilon_0 E}{\hbar}[\varepsilon(E) - 1] \quad (5)$$

$$\sigma^F(E) = \sigma_1^F(E) + i\sigma_2^F(E) \equiv \sigma(E)d \quad (6)$$

where σ is the complex optical conductivity; E is the photon energy; $\hbar$ is the reduced Planck constant; ε is the complex dielectric function; ε_0 is the vacuum permittivity; and σ^F is the complex film conductivity. As shown in Figure 4a, the σ_1^F of 1L-MoS_2, graphene/MoS_2 and graphene/h-BN/MoS_2 films are in the form of step function, implying that the 1L-MoS_2 layers can maintain direct band gap transition character even in the graphene/h-BN/MoS_2 heterostructures.[60] The MoS_2 layer may absorb or emit light with high efficiency (i.e., strong light−matter interaction), suggesting the superiority of graphene/h-BN/MoS_2 heterostructures applied in optoelectronic devices with high quantum efficiency. Moreover, graphene/h-BN/MoS_2 and graphene/MoS_2 have higher σ_1^F compared to that of graphene/h-BN, 1L-graphene, or 1L-MoS_2. Referring to the transmittance of the 1L-graphene (Figure S6a, Supporting Information), the absorption 1L-graphene is lower than 3% in a wide wavelength region; thus, it is the MoS_2 layers in the heterostructures that played the role of light absorption in the heterostructure. The photogenerated electron−hole pairs separated effectively at the MoS_2−graphene interface (revealed by the Raman and PL spectral analysis results mentioned above), coupled with the high electron mobility of graphene, so that the photogenerated electrons can be transmitted quickly in graphene/MoS_2. Eventually, the electrons contributed to the overall σ_1^F, improving the full-band σ_1^F response. As a result, graphene/MoS_2 heterostructures can be used for high-gain light detection. Furthermore, the σ_1^F slightly improved after 1L-h-BN insertion, suggesting that the 1L-h-BN blocking strength on electrons from MoS_2 is very limited. It should be noted that in the σ_1^F of graphene/h-BN/MoS_2 heterostructure, the dielectric screening effect from the injected h-BN on the charge impurities from the lower interfaces can depress the scattering effect and increase the carrier mobility,[48] which may contribute to the improvement of the optical conductivity. Besides the 1L-h-BN absorption edge at around 6.1 eV, the graphene/h-BN conductivity is basically consistent with 1L-graphene, demonstrating that 1L-h-BN will not supply electrons to graphene or largely improve the carrier mobility of graphene. Assuming that the 1L-h-BN blocked a large fraction of the photogenerated electrons form MoS_2, referring to the relationship between σ_1^F, carrier mobility, and concentrations of the optical injected charged carriers from a previous study,[57] the σ_1^F is supposed to reduced. This was not observed in the sense proving that 1L-h-BN has weak blocking ability.

As announced previously, the optical conductivity of graphene layers has been proved that cannot been described specifically by interband transitions but the plasmonic excitation.[61] To shed light on this kind of collective excitation in graphene layers, we studied the energy-loss function $\mathrm{Im}(\varepsilon^{-1})$ in detail. As shown in Figure 4b, the $\mathrm{Im}(\varepsilon^{-1})$ of 1L-graphene has been investigated in a previous study:[58,61,62] the feature at around 4.6 eV can be attributed to saddle-point resonance absorption near M point in BZ. The structures at 5.5 eV are corresponding to the π in-plane plasmon modes. The absorption peaks in the higher photon energy range are reported from $\pi + \sigma$ in-plane plasmon modes. Then, the broad plasmon excitation background can be attributed to the transition around the Dirac cone (π to π^* around the K point in the BZ). Comparing the $\mathrm{Im}(\varepsilon^{-1})$ of graphene/h-BN and graphene/MoS_2, and the graphene shows better photoelectric properties when encapsulated by h-BN.

Here, we concentrated on monitoring the evolution of the plasmon excitations of graphene layers in the two heterostructures. After being covered by 1L-MoS_2, the plasmon excitation features still exist, along with a decreasing intensity in the low and high photon energy region. This can be explained by the fact that the electron injection from MoS_2 increased the efficient dielectric screening on the electrons in

https://doi.org/10.1021/acsami.2c20100
ACS Appl. Mater. Interfaces 2023, 15, 2468−2478

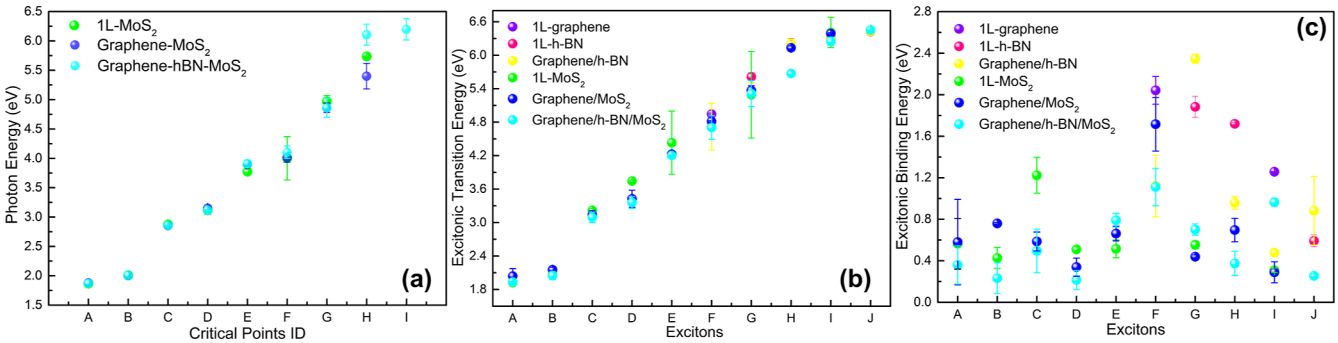

Figure 5. (a) CP transition energies E_{th}, (b) exciton transition energies E_0, and (c) binding energies E_b of the samples. The specific values are listed in Supporting Information Tables S3−S9.

the graphene layer, which decreased the long-distance electron−electron Coulombic interaction. Then, in graphene/h-BN/MoS_2, the 1L-h-BN barrier layer weakly blocked the electron injection and reduced the dielectric screening effect, as a consequence that the large range Im(ε^{-1}) improved in comparison with that of graphene/MoS_2. Notably, the 1L-h-BN has no obvious plasmonic excitations. Thus, h-BN did not contribute to the Im(ε^{-1}) of graphene/h-BN or graphene/h-BN/MoS_2.

2.4. Electronic Band Structures and Excitons. The optical properties of a 2D material system are determined by its electronic band structures and exciton states. The evolution of the electronic band structures can be determined by studying the direct interband transitions, that is, CPs. The properties of CPs and excitons can be derived by the standard critical point (SCP) model[54,57,63] and Broaden Lorentz line shape model,[32,64] respectively. The detailed fitting process and the specific fitting parameters are introduced in Supporting Information (Figures S7, S8 and Tables S3, S9). Here, we reported the CP transition energies (E_{th}, Figure 5a), excitonic transition energies (E_0, Figure 5b), and excitonic binding energies (E_b, Figure 5c) in the photon energy range from 1.2−6.5 eV of the samples. As aforementioned, the optical absorption of graphene cannot be accurately described by interband transitions; thus, only the CPs in MoS_2 layers in 1L-MoS_2, graphene/MoS_2 and graphene/h-BN/MoS_2 samples were calculated.

As shown in Figure 5a, the E_{th} of the CPs in the graphene/MoS_2 and graphene/h-BN/MoS_2 basically unchanged comparing with those of 1L-MoS_2 films. This implies that the electronic band structure of MoS_2 was not affected by either graphene or h-BN. That is to say, the interlayer hybridization was generally weak in these two heterostructures, which can be attributed to the incommensurate interfaces of MoS_2, graphene, or h-BN.[6] Whether a heterostructure system meets a commensurate state depends on the lattice constants of the component layers. Even if a commensurate system can transition to an incommensurate system by varying the interlayer lattice angle or adding additional layers on this heterostructure.[65] For incommensurate or non-lattice matched systems, the interlayer hybridization degree will be less pronounced.[6] With regard to our CVD synthesized 2D material films and layer-by-layer transferring stacked heterostructures, as well as the mismatched lattice constants, it can be reasonably speculated to be an incommensurate system. Then, the degree of interlayer hybridization is very weak, as revealed by the unchanged CP transition energies. Besides, the inherent band gap energies of these three 2D materials are very different, also leading to the negligible hybridization on the band structure.[66] The unchanged electronic band structure of MoS_2 in graphene/MoS_2 was predicted by previous studies using density functional theory, where the electron energy levels showed a simple superposition.[14] Hence, the graphene Dirac cone had not been altered;[67,68] in the meantime, the direct band gap of MoS_2 can also be retained (consistent with our previous optical conductivity results). With 1L-MoS_2 layers acting as efficient optical absorption layers, graphene layers serve as excellent carrier transport layers, and graphene/MoS_2 and graphene/h-BN/MoS_2 heterostructures hold great promise in ultrahigh-gain photodetectors.

Figure 5b−c, respectively, depicts the excitonic transition energies E_0 and binding energies E_b of the samples; the specific values are listed in Supporting Information Tables S4−S9. The excitons in 1L-graphene,[58,61,62] 1L-MoS_2,[57] and 1L-h-BN[69−71] have been investigated in previous studies. Here, we pay more attention to the modulation effects of stacking graphene/MoS_2 and graphene/h-BN/MoS_2. As shown in Figure 5b,c, the E_0 of graphene and MoS_2 layers slightly redshifted in the heterostructures, as well as the E_b. This can be explained by the increased dielectric screening in heterostructures, which is consistent with the results in WS_2/MoS_2 heterostructures.[57] Besides, the build-in strain (induced by stacking heterostructures) and electron injection from MoS_2 also decreased plasmon excitation energies (E_0) of graphene.[61] However, the E_0 and E_b of the MoS_2 in the heterostructures only slightly shifted, implying that the photodetectors based on graphene/MoS_2 and graphene/h-BN/MoS_2 can still respond at the original wavelength as the 1L-MoS_2 devices. This is attributed to the very limited screening distance of graphene (only ∼5 Å, as reported previously[72]), largely shorter than that of MoS_2 (∼6−10 nm[18]). Then, we studied the 1L-h-BN insertion effects on exitonic properties of the MoS_2 layer. As we can see, the E_0 and E_b of the MoS_2 layers in graphene/h-BN/MoS_2 slightly redshifted. Especially, E_b significantly redshifted due to the released quantum confinement effect, where some outliers may be caused by the calculation error. This also demonstrated that the interlayer coupling effect had not been largely reduced by 1L-h-BN, agreeing with the results in the PL section. Investigated by previous studies, the 1L-h-BN adjacent layer alters the efficient dielectric screening effects on the MoS_2 layer. With regard to the MoS_2/h-BN bilayer, comparing with the MoS_2 monolayer, the dielectric screening effect is enhanced, resulting in the increasing exciton dissociation rate.[52] However, in our previous work about WS_2/h-BN/MoS_2,[32] the 1L-h-BN insertion decreases the efficient dielectric screening because of the strong dielectric screening effect

https://doi.org/10.1021/acsami.2c20100
ACS Appl. Mater. Interfaces 2023, 15, 2468−2478

introduced by WS_2 on MoS_2. Additionally, the dielectric screening effect plays a leading part modulating the excitonic properties of WS_2/h-BN/MoS_2 heterostructures. Consequently, the excitonic binding energies blueshift in WS_2/h-BN/MoS_2. On the contrary, with regard to the graphene/h-BN/MoS_2 heterostructure, the dielectric screening modulation of 1L-h-BN insertion played a minor role compared with the releasing quantum confinement effect due to the limited dielectric screening strength of graphene on MoS_2. Eventually, the excitonic binding energies redshift as a result of the releasing quantum confinement effect in graphene/h-BN/MoS_2 heterostructures, as shown in Figure 5c.

3. CONCLUSIONS

In this work, based on graphene/h-BN/MoS_2 heterostructures, the modulation effects of the 1L-h-BN barrier layer on the electronic band structures and exciton properties were experimentally revealed. By Raman and PL spectra analyses, we found that 1L-h-BN insertion only partly blocked the interlayer carrier transfer, while reduced the interlayer coupling effects, by decreasing the efficient dielectric screening and releasing the quantum confinement. Moreover, the graphene/h-BN/MoS_2 presents higher amplitude of optical conductivity and plasmon excitation, compared with those of graphene/MoS_2 counterparts. This may benefit from the dielectric screening effect of the 1L-h-BN barrier layer on the charged impurities on the lower interfaces or substrates. Furthermore, by monitoring the evolution of the CP transition energies, we found that the electronic band structures of MoS_2 layers in neither the graphene/MoS_2 nor graphene/h-BN/MoS_2 went through negligible hybridization. This can be attributed to the incommensurate interfaces of MoS_2, graphene, or h-BN, as well as the large band gap energy differences between them. Hence, the direct interband transition character of MoS_2 and the Dirac cone of graphene can be remained in graphene/MoS_2 and graphene/h-BN/MoS_2, guaranteeing the efficient optical absorption and high mobility of the heterostructures, respectively. Thus, the photodetectors based on these two heterostructures can possess ultrahigh optical gain. Finally, the exciton binding energies and transition energies slightly redshift caused by the released quantum confinement. Our results experimentally unveiled the insertion effects of the 1L-hBN barrier layer, which will be beneficial to the exploitation of new concept and highly efficient optoelectronic applications based on the tunneling heterostructures.

4. EXPERIMENTAL SECTION

4.1. Preparation of Heterostructure Thin Films. To fabricate the graphene/MoS_2 and graphene/h-BN/MoS_2 heterostructures, high-quality and large-size 1L-graphene, 1L-h-BN, and 1L-MoS_2 thin films were synthesized using the CVD method. The synthesis process was assisted by SixCarbon Technology Shenzhen. 1L-MoS_2 (1 cm × 1 cm) continuous films were synthesized on SiO_2/Si substrates, where the MoO_3 powder and pure sulfur powder were used as precursor and reactant materials, respectively. 1L-Graphene (1 cm × 1 cm) continuous films were deposited on cooper foil by alternating the flow of methane (CH_4) and hydrogen (H_2). 1L-h-BN (1 cm × 1 cm) continuous films were synthesized on copper foil using borane as the precursor. The basic growth conditions of these films were similar to those previously reported;[73−75] thus, we would not describe in detail here. With the use of a wet transfer process (PMMA carrying layer method) similar to that described in previous studies,[76] the as-grown monolayer samples were easily transferred onto *c*-plane (0001) sapphire substrates for following spectral measurements and surface topography characterization. As for multilayer heterostructures, a layer-by-layer transfer process was implemented. Each transfer operation was followed by the same annealing treatment (vacuum degree ∼ 0.1 Pa, 350 °C, 2 h), in order to remove the interface impurities as far as possible to produce smooth films with good interlayer coupling. This is crucial for accurate analysis of the interlayer coupling strength and exciton luminescence, especially interlayer excitons.[32]

4.2. Surface Topography Characterization of the Thin Films. The morphological characterization of 1L-samples and heterostructures were carried out by using the AFM (AIST-NT System) in the contact mode, from which the surface roughness of the samples was evaluated. Moreover, the optical microscopy images were all shot using the optical microscope (Guangzhou Mingmei, MJ31).

4.3. Optical Spectroscopy Tests. Raman and PL (SPEX/403) spectra were carried out at room temperature under 532 nm laser excitation. The room-temperature transmission spectra of our samples were measured using a spectrophotometer (Jinghua UV1901) within the wavelength range from 360 to 1100 nm in air. The optical properties of the samples were investigated by SE (J. A. Woollam, Inc. M2000X-FB-300XTF) at room temperature. The ellipsometric data (ψ, Δ) were collected over a wavelength range from 200 to 1000 nm (513 groups of data points) at a fixed incident angle of 65°.

■ ASSOCIATED CONTENT

Supporting Information

The Supporting Information is available free of charge at https://pubs.acs.org/doi/10.1021/acsami.2c20100.

> Additional experimental data on the surface topography characterization; Raman and PL spectra and SE including AFM results and the optical microscopy images; Raman and PL spectra and detailed multi-peak fitting results; SE fitting and *K*−*K* consistency check process; specific SCP model and Broadened Lorentz line shape fitting parameters (CP and exciton properties) (DOCX)

■ AUTHOR INFORMATION

Corresponding Authors

Shaojuan Li − *State Key Laboratory of Applied Optics, Changchun Institute of Optics, Fine Mechanics and Physics, Chinese Academy of Sciences, Changchun 130033, China;* orcid.org/0000-0002-0504-2934; Email: lishaojuan@ciomp.ac.cn

Rongjun Zhang − *Shanghai Frontiers Science Research Base of Intelligent Optoelectronics and Proception, Institute of Optoelectronics, Fudan University, Shanghai 200433, China; School of Information Science and Engineering and Academy for Engineering & Technology, Fudan University, Shanghai 200433, China*; Email: rjzhang@fudan.edu.cn

Authors

Xudan Zhu − *Shanghai Frontiers Science Research Base of Intelligent Optoelectronics and Proception, Institute of Optoelectronics, Fudan University, Shanghai 200433, China; State Key Laboratory of Applied Optics, Changchun Institute of Optics, Fine Mechanics and Physics, Chinese Academy of Sciences, Changchun 130033, China;* orcid.org/0000-0002-1605-6047

Junbo He − *School of Information Science and Engineering, Fudan University, Shanghai 200433, China*

Weiming Liu − *School of Information Science and Engineering, Fudan University, Shanghai 200433, China*

https://doi.org/10.1021/acsami.2c20100
ACS Appl. Mater. Interfaces 2023, 15, 2468−2478

Yuxiang Zheng − *School of Information Science and Engineering, Fudan University, Shanghai 200433, China;* orcid.org/0000-0002-9116-4849

Chuanxiang Sheng − *School of Information Science and Engineering, Fudan University, Shanghai 200433, China;* orcid.org/0000-0001-7821-0014

Yi Luo − *Microsystem and Terahertz Research Center, Chengdu 610200, China*

Junhao Chu − *Shanghai Frontiers Science Research Base of Intelligent Optoelectronics and Proception, Institute of Optoelectronics, Fudan University, Shanghai 200433, China*

Complete contact information is available at: https://pubs.acs.org/10.1021/acsami.2c20100

Author Contributions

X.Z. carried out the SE, PL, and Raman experiments and analyzed the data. J.H. and W.L. contributed in the data fitting process. Y.Z. and C.S. provided guidance in the analysis on CPs and excitons. Y.L., S.L., R.Z., and J.C. made contributions to project administration, funding acquisition, supervision and manuscript writing and revising. All authors discussed the results and commented on the manuscript. All authors have given approval to the final version of the manuscript

Notes

The authors declare no competing financial interest.

■ ACKNOWLEDGMENTS

The work was financially supported by the National Natural Science Foundation of China (nos. 11674062, 62022081, and 61974099), NSAF (Grant No. U2230108), the National Key R&D Program of China (2021YFB2012601), the Fudan University-CIOMP Joint Fund (FC2019-006), the State Key Laboratory of Applied Optics (SKLAO2022001A16), the Natural Science Foundation of Jilin Province (20210101173JC), and the Changchun Key Research and Development Program (21ZY03).

■ REFERENCES

(1) Xia, F.; Wang, H.; Xiao, D.; Dubey, M.; Ramasubramaniam, A. Two-Dimensional Material Nanophotonics. *Nat. Photonics* **2014**, *8*, 899−907.

(2) An, J.; Zhao, X.; Zhang, Y.; Liu, M.; Yuan, J.; Sun, X.; Zhang, Z.; Wang, B.; Li, S.; Li, D. Perspectives of 2D Materials for Optoelectronic Integration. *Adv. Funct. Mater.* **2021**, *32*, 2110119.

(3) Cong, C.; Shang, J.; Wang, Y.; Yu, T. Optical Properties of 2D Semiconductor WS2. *Adv. Opt. Mater.* **2018**, *6*, 1700767.

(4) Raja, A.; Chaves, A.; Yu, J.; Arefe, G.; Hill, H. M.; Rigosi, A. F.; Berkelbach, T. C.; Nagler, P.; Schüller, C.; Korn, T.; Nuckolls, C.; Hone, J.; Brus, L. E.; Heinz, T. F.; Reichman, D. R.; Chernikov, A. Coulomb Engineering of the Bandgap and Excitons in Two-Dimensional Materials. *Nat. Commun.* **2017**, *8*, 15251.

(5) Noori, K.; Cheng, N. L. Q.; Xuan, F.; Quek, S. Y. Dielectric Screening by 2D Substrates. *2D Mater.* **2019**, *6*, 035036.

(6) Winther, K. T.; Thygesen, K. S. Band structure engineering in van der Waals heterostructures via dielectric screening: the GΔW method. *2D Mater.* **2017**, *4*, 025059.

(7) Kretinin, A. V.; Cao, Y.; Tu, J. S.; Yu, G. L.; Jalil, R.; Novoselov, K. S.; Haigh, S. J.; Gholinia, A.; Mishchenko, A.; Lozada, M.; Georgiou, T.; Woods, C. R.; Withers, F.; Blake, P.; Eda, G.; Wirsig, A.; Hucho, C.; Watanabe, K.; Taniguchi, T.; Geim, A. K.; Gorbachev, R. V. Electronic Properties of Graphene Encapsulated with Different Two-Dimensional Atomic Crystals. *Nano Lett.* **2014**, *14*, 3270−3276.

(8) Ezhilmaran, B.; Patra, A.; Benny, S.; Sreelakshmi, M. R.; Akshay, V. V. A.; Bhat, S. V.; Rout, C. S. Recent Developments in the Photodetector Applications of Schottky Diodes Based on 2D Materials. *J. Mater. Chem. C* **2021**, *9*, 6122−6150.

(9) Li, H.; Li, X.; Park, J.-H.; Tao, L.; Kim, K. K.; Lee, Y. H.; Xu, J.-B. Restoring the Photovoltaic Effect in Graphene-Based Van Der Waals Heterojunctions Towards Self-Powered High-Detectivity Photodetectors. *Nano Energy* **2019**, *57*, 214−221.

(10) Zhang, W.; Chuu, C. P.; Huang, J. K.; Chen, C. H.; Tsai, M. L.; Chang, Y. H.; Liang, C. T.; Chen, Y. Z.; Chueh, Y. L.; He, J. H.; Chou, M. Y.; Li, L. J. Ultrahigh-Gain Photodetectors Based on Atomically Thin Graphene-MoS2 Heterostructures. *Sci. Rep.* **2014**, *4*, 3826.

(11) Gao, S.; Wang, Z.; Wang, H.; Meng, F.; Wang, P.; Chen, S.; Zeng, Y.; Zhao, J.; Hu, H.; Cao, R.; Xu, Z.; Guo, Z.; Zhang, H. Graphene/MoS 2 /Graphene Vertical Heterostructure-Based Broadband Photodetector with High Performance. *Adv. Opt. Mater.* **2020**, *8*, 2001730.

(12) Beckmann, Y.; Grundmann, A.; Daniel, L.; Abdelbaky, M.; McAleese, C.; Wang, X.; Conran, B.; Pasko, S.; Krotkus, S.; Heuken, M.; Kalisch, H.; Vescan, A.; Mertin, W.; Kümmell, T.; Bacher, G. Role of Surface Adsorbates on the Photoresponse of (MO)CVD-Grown Graphene-MoS2 Heterostructure Photodetectors. *ACS Appl. Mater. Interfaces* **2022**, *14*, 35184−35193.

(13) Jiang, Y.; Miao, L.; Jiang, G.; Chen, Y.; Qi, X.; Jiang, X. F.; Zhang, H.; Wen, S. Broadband and enhanced nonlinear optical response of MoS2/graphene nanocomposites for ultrafast photonics applications. *Sci. Rep.* **2015**, *5*, 16372.

(14) Bernardi, M.; Palummo, M.; Grossman, J. C. Extraordinary Sunlight Absorption and One Nanometer Thick Photovoltaics Using Two-Dimensional Monolayer Materials. *Nano Lett.* **2013**, *13*, 3664−3670.

(15) Long, H.; Harley-Trochimczyk, A.; Pham, T.; Tang, Z.; Shi, T.; Zettl, A.; Carraro, C.; Worsley, M. A.; Maboudian, R. High Surface Area MoS2/Graphene Hybrid Aerogel for Ultrasensitive NO2Detection. *Adv. Funct. Mater.* **2016**, *26*, 5158−5165.

(16) Wang, H.; Tran, D.; Qian, J.; Ding, F.; Losic, D. MoS 2 /Graphene Composites as Promising Materials for Energy Storage and Conversion Applications. *Adv. Mater. Interfaces* **2019**, *6*, 1900915.

(17) Bartolomeo, A. D. Graphene Schottky Diodes: An Experimental Review of the Rectifying Graphene/Semiconductor Heterojunction. *Phys. Rep.* **2016**, *606*, 1−58.

(18) Li, Y.; Xu, C. Y.; Qin, J. K.; Feng, W.; Wang, J. Y.; Zhang, S.; Ma, L. P.; Cao, J.; Hu, P. A.; Ren, W.; Zhen, L. Tuning the Excitonic States in MoS2/Graphene van der Waals Heterostructures via Electrochemical Gating. *Adv. Funct. Mater.* **2016**, *26*, 293−302.

(19) Shih, C. J.; Wang, Q. H.; Son, Y.; Jin, Z.; Blankschtein, D.; Strano, M. S. Tuning On-Off Current Ratio and Field-Effect Mobility in a MoS2-Graphene Heterostructure via Schottky Barrier Modulation. *ACS Nano* **2014**, *8*, 5790−5798.

(20) Qiao, H.; Huang, Z.; Ren, X.; Liu, S.; Zhang, Y.; Qi, X.; Zhang, H. Self-Powered Photodetectors Based on 2D Materials. *Adv. Opt. Mater.* **2019**, *8*, 1900765.

(21) Withers, F.; Del Pozo-Zamudio, O.; Mishchenko, A.; Rooney, A. P.; Gholinia, A.; Watanabe, K.; Taniguchi, T.; Haigh, S. J.; Geim, A. K.; Tartakovskii, A. I.; Novoselov, K. S. Light-Emitting Diodes by Band-Structure Engineering in Van Der Waals Heterostructures. *Nat. Mater.* **2015**, *14*, 301−306.

(22) Wang, J.; Yao, Q.; Huang, C. W.; Zou, X.; Liao, L.; Chen, S.; Fan, Z.; Zhang, K.; Wu, W.; Xiao, X.; Jiang, C.; Wu, W. W. High Mobility MoS2 Transistor with Low Schottky Barrier Contact by Using Atomic Thick h-BN as a Tunneling Layer. *Adv. Mater.* **2016**, *28*, 8302−8308.

(23) Ahmed, T.; Roy, K.; Kakkar, S.; Pradhan, A.; Ghosh, A. Interplay of charge transfer and disorder in optoelectronic response in Graphene/hBN/MoS2 van der Waals heterostructures. *2D Mater.* **2020**, *7*, 025043.

(24) Zan, W.; Geng, W.; Liu, H.; Yao, X. Electric-field and strain-tunable electronic properties of MoS2/h-BN/graphene vertical heterostructures. *Phys. Chem. Chem. Phys.* **2016**, *18*, 3159−3164.

(25) Liu, B.; Zhao, Y. Q.; Yu, Z. L.; Wang, L. Z.; Cai, M. Q. Tuning the Schottky Rectification in Graphene-Hexagonal Boron Nitride-Molybdenum Disulfide Heterostructure. *J. Colloid Interface Sci.* **2018**, *513*, 677−683.
(26) Vu, Q. A.; Lee, J. H.; Nguyen, V. L.; Shin, Y. S.; Lim, S. C.; Lee, K.; Heo, J.; Park, S.; Kim, K.; Lee, Y. H.; Yu, W. J. Tuning Carrier Tunneling in Van Der Waals Heterostructures for Ultrahigh Detectivity. *Nano Lett.* **2017**, *17*, 453−459.
(27) Sundararaju, U.; Mohammad Haniff, M. A. S.; Ker, P. J.; Menon, P. S. MoS2/h-BN/Graphene Heterostructure and Plasmonic Effect for Self-Powering Photodetector: A Review. *Materials* **2021**, *14*, 1672.
(28) Li, C.; Yan, X.; Bao, W.; Ding, S.; Zhang, D. W.; Zhou, P. Low sub-threshold swing realization with contacts of graphene/h-BN/MoS2 heterostructures in MoS2 transistors. *Appl. Phys. Lett.* **2017**, *111*, 193502.
(29) Vu, Q. A.; Shin, Y. S.; Kim, Y. R.; Nguyen, V. L.; Kang, W. T.; Kim, H.; Luong, D. H.; Lee, I. M.; Lee, K.; Ko, D. S.; Heo, J.; Park, S.; Lee, Y. H.; Yu, W. J. Two-Terminal Floating-Gate Memory with Van Der Waals Heterostructures for Ultrahigh On/off Ratio. *Nat. Commun.* **2016**, *7*, 12725.
(30) Jeong, H.; Oh, H. M.; Bang, S.; Jeong, H. J.; An, S. J.; Han, G. H.; Kim, H.; Yun, S. J.; Kim, K. K.; Park, J. C.; Lee, Y. H.; Lerondel, G.; Jeong, M. S. Metal-Insulator-Semiconductor Diode Consisting of Two-Dimensional Nanomaterials. *Nano Lett.* **2016**, *16*, 1858−1862.
(31) He, J.; Zhu, X.; Liu, W.; Hu, E.; Wang, J.; Zhang, R. Versatile band structure and electron-phonon coupling in layered PtSe2 with strong interlayer interaction. *Nano Res.* **2022**, *15*, 6613−6619.
(32) Zhu, X.; He, J.; Zhang, R.; Cong, C.; Zheng, Y.; Zhang, H.; Wang, S.; Zhao, H.; Zhu, M.; Zhang, S.; Li, S.; Chen, L. Effects of interlayer coupling on the excitons and electronic structures of WS2/hBN/MoS2 van der Waals heterostructures. *Nano Res.* **2022**, *15*, 2674−2681.
(33) Yu, P. Y.; Cardona, M.*Fundamentals of Semiconductors: Physics and Materials Properties*, 4th ed.; Springer: Springer HeidelbergDordrecht London New York, 2010; p 788.
(34) Grundmann, M.*The Physics of Semiconductors*; Springer: Berlin Heidelberg, 2006; Vol. *543210*, p 273.
(35) Lee, C.; Yan, H.; Brus, L. E.; Heinz, T. F.; Hone, J.; Ryu, S. Anomalous Lattice Vibrations of Single- and Few-Layer MoS2. *ACS Nano* **2010**, *4*, 2695−2700.
(36) Das, A.; Pisana, S.; Chakraborty, B.; Piscanec, S.; Saha, S. K.; Waghmare, U. V.; Novoselov, K. S.; Krishnamurthy, H. R.; Geim, A. K.; Ferrari, A. C.; Sood, A. K. Monitoring Dopants by Raman Scattering in an Electrochemically Top-Gated Graphene Transistor. *Nat. Nanotechnol.* **2008**, *3*, 210−215.
(37) Ferrari, A. C.; Basko, D. M. Raman Spectroscopy as a Versatile Tool for Studying the Properties of Graphene. *Nat. Nanotechnol.* **2013**, *8*, 235−246.
(38) Pisana, S.; Lazzeri, M.; Casiraghi, C.; Novoselov, K. S.; Geim, A. K.; Ferrari, A. C.; Mauri, F. Breakdown of the Adiabatic Born-Oppenheimer Approximation in Graphene. *Nat. Mater.* **2007**, *6*, 198−201.
(39) Cai, Q.; Scullion, D.; Falin, A.; Watanabe, K.; Taniguchi, T.; Chen, Y.; Santos, E. J.; Li, L. H. Raman Signature and Phonon Dispersion of Atomically Thin Boron Nitride. *Nanoscale* **2017**, *9*, 3059−3067.
(40) Tran, M. D.; Kim, H.; Kim, J. S.; Doan, M. H.; Chau, T. K.; Vu, Q. A.; Kim, J. H.; Lee, Y. H. Two-Terminal Multibit Optical Memory Via Van Der Waals Heterostructure. *Adv. Mater.* **2019**, *31*, No. e1807075.
(41) Li, H.; Zhang, Q.; Yap, Y.; Tay, B. K.; Edwin, T. H. T.; Olivier, A.; Baillargeat, D. From Bulk to Monolayer MoS2: Evolution of Raman Scattering. *Adv. Funct. Mater.* **2012**, *22*, 1385−1390.
(42) Liang, L.; Meunier, V. First-principles Raman spectra of MoS2, WS2 and their heterostructures. *Nanoscale* **2014**, *6*, 5394.
(43) Waldecker, L.; Raja, A.; Rösner, M.; Steinke, C.; Bostwick, A.; Koch, R. J.; Jozwiak, C.; Taniguchi, T.; Watanabe, K.; Rotenberg, E.; Wehling, T. O.; Heinz, T. F. Rigid Band Shifts in Two-Dimensional Semiconductors through External Dielectric Screening. *Phys. Rev. Lett.* **2019**, *123*, 206403.
(44) Gao, S.; Yang, L.; Spataru, C. D. Interlayer Coupling and Gate-Tunable Excitons in Transition Metal Dichalcogenide Heterostructures. *Nano Lett.* **2017**, *17*, 7809−7813.
(45) Yang, M.; Wang, L.; Hu, G.; Chen, X.; Gong, P. L.; Cong, X.; Liu, Y.; Yang, Y.; Li, X.; Zhao, X.; Liu, X. Optical Identification of Interlayer Coupling of Graphene/MoS_2 Van Der Waals Heterostructures. *Nano Res.* **2021**, *14*, 2241−2246.
(46) Wang, S.; Wang, X.; Warner, J. H. All Chemical Vapor Deposition Growth of MoS2:h-BN Vertical van der Waals Heterostructures. *ACS Nano* **2015**, *9*, 5246−5254.
(47) Huang, Z.; He, C.; Qi, X.; Yang, H.; Liu, W.; Wei, X.; Peng, X.; Zhong, J. Band Structure Engineering of Monolayer MoS_2 on h-BN: First-Principles Calculations. *J. Phys. D: Appl. Phys.* **2014**, *47*, 075301.
(48) Behura, S.; Nguyen, P.; Che, S.; Debbarma, R.; Berry, V. Large-Area, Transfer-Free, Oxide-Assisted Synthesis of Hexagonal Boron Nitride Films and Their Heterostructures with MoS2 and WS2. *J. Am. Chem. Soc.* **2015**, *137*, 13060−13065.
(49) Tran, M. D.; Kim, J. H.; Lee, Y. H. Tailoring Photoluminescence of Monolayer Transition Metal Dichalcogenides. *Curr. Appl. Phys.* **2016**, *16*, 1159−1174.
(50) Cong, C.; Zou, C.; Cao, B.; Wu, L.; Shang, J.; Wang, H.; Qiu, Z.; Hu, L.; Tian, P.; Liu, R.; Yu, T. Intrinsic excitonic emission and valley Zeeman splitting in epitaxial MS2 (M = Mo and W) monolayers on hexagonal boron nitride. *Nano Res.* **2018**, *11*, 6227−6236.
(51) Courtade, E.; Han, B.; Nakhaie, S.; Robert, C.; Marie, X.; Renucci, P.; Taniguchi, T.; Watanabe, K.; Geelhaar, L.; Lopes, J. M. J.; Urbaszek, B. Spectrally narrow exciton luminescence from monolayer MoS2 and MoSe2 exfoliated onto epitaxially grown hexagonal BN. *Appl. Phys. Lett.* **2018**, *113*, 032106.
(52) Florian, M.; Hartmann, M.; Steinhoff, A.; Klein, J.; Holleitner, A. W.; Finley, J. J.; Wehling, T. O.; Kaniber, M.; Gies, C. The Dielectric Impact of Layer Distances on Exciton and Trion Binding Energies in Van Der Waals Heterostructures. *Nano Lett.* **2018**, *18*, 2725−2732.
(53) Zhu, X.; Li, D.; Zhang, R.; Zhang, H.; Cong, C.; Zhu, M.; Shi, Y.; Wu, Y.; Wang, S.; Zheng, Y.; Chen, L. Probing quantum confinement effects on the excitonic property and electronic band structures of MoS2. *Appl. Surf. Sci.* **2020**, *519*, 146262.
(54) Park, J. W.; So, H. S.; Kim, S.; Choi, S.-H.; Lee, H.; Lee, J.; Lee, C.; Kim, Y. Optical properties of large-area ultrathin MoS2 films: Evolution from a single layer to multilayers. *J. Appl. Phys.* **2014**, *116*, 183509.
(55) Molina-Sánchez, A.; Sangalli, D.; Hummer, K.; Marini, A.; Wirtz, L. Effect of Spin-Orbit Interaction on the Optical Spectra of Single-Layer, Double-Layer, and Bulk MoS_2. *Phys. Rev. B: Condens. Matter Mater. Phys.* **2013**, *88*, 045412.
(56) He, K.; Poole, C.; Mak, K. F.; Shan, J. Experimental Demonstration of Continuous Electronic Structure Tuning via Strain in Atomically Thin MoS2. *Nano Lett.* **2013**, *13*, 2931−2936.
(57) Zhu, X.; He, J.; Zhang, R.; Cong, C.; Zheng, Y.; Zhang, H.; Zhang, S.; Chen, L. Effects of dielectric screening on the excitonic and critical points properties of WS2/MoS2 heterostructures. *Nanoscale* **2020**, *12*, 23732−23739.
(58) Li, W.; Cheng, G.; Liang, Y.; Tian, B.; Liang, X.; Peng, L.; Hight Walker, A. R.; Gundlach, D. J.; Nguyen, N. V. Broadband Optical Properties of Graphene by Spectroscopic Ellipsometry. *Carbon* **2016**, *99*, 348−353.
(59) Li, Y.; Chernikov, A.; Zhang, X.; Rigosi, A.; Hill, H. M.; van der Zande, A. M. v. d.; Chenet, D. A.; Shih, E.-M.; Hone, J.; Heinz, T. F. Measurement of the optical dielectric function of monolayer transition-metal dichalcogenides:MoS2,MoSe2,WS2, andWSe2. *Phys. Rev. B* **2014**, *90*, 205422.
(60) Mak, K. F.; Lee, C.; Hone, J.; Shan, J.; Heinz, T. F. Atomically Thin MoS_2: A New Direct-Gap Semiconductor. *Phys. Rev. Lett.* **2010**, *105*, 136805.

https://doi.org/10.1021/acsami.2c20100
ACS Appl. Mater. Interfaces 2023, 15, 2468−2478

(61) Santoso, I.; Gogoi, P. K.; Su, H. B.; Huang, H.; Lu, Y.; Qi, D.; Chen, W.; Majidi, M. A.; Feng, Y. P.; Wee, A. T. S.; Loh, K. P.; Venkatesan, T.; Saichu, R. P.; Goos, A.; Kotlov, A.; Rübhausen, M.; Rusydi, A. Observation of Room-Temperature High-Energy Resonant Excitonic Effects in Graphene. *Phys. Rev. B* **2011**, *84*, 081403R.
(62) Li, P.; Ren, X.; He, L. First-Principles Calculations and Model Analysis of Plasmon Excitations in Graphene and Graphene/hBN Heterostructure. *Phys. Rev. B* **2017**, *96*, 165417.
(63) Li, W.; Birdwell, A. G.; Amani, M.; Burke, R. A.; Ling, X.; Lee, Y. H.; Liang, X.; Peng, L.; Richter, C. A.; Kong, J.; Gundlach, D. J.; Nguyen, N. V. Broadband optical properties of large-area monolayer CVD molybdenum disulfide. *Phys. Rev. B* **2014**, *90*, 195434.
(64) Muth, J. F.; Kolbas, R. M.; Sharma, A. K.; Oktyabrsky, S.; Narayan, J. Excitonic Structure and Absorption Coefficient Measurements of ZnO Single Crystal Epitaxial Films Deposited by Pulsed Laser Deposition. *J. Appl. Phys.* **1999**, *85*, 7884−7887.
(65) Woods, C. R.; Britnell, L.; Eckmann, A.; Ma, R. S.; Lu, J. C.; Guo, H. M.; Lin, X.; Yu, G. L.; Cao, Y.; Gorbachev, R. V.; Kretinin, A. V.; Park, J.; Ponomarenko, L. A.; Katsnelson, M. I.; Gornostyrev, Y. N.; Watanabe, K.; Taniguchi, T.; Casiraghi, C.; Gao, H. J.; Geim, A. K.; Novoselov, K. S. Commensurate-incommensurate transition in graphene on hexagonal boron nitride. *Nat. Phys.* **2014**, *10*, 451−456.
(66) Le, N. B.; Huan, T. D.; Woods, L. M. Interlayer Interactions in Van Der Waals Heterostructures: Electron and Phonon Properties. *ACS Appl. Mater. Interfaces* **2016**, *8*, 6286−6292.
(67) Lu, C. P.; Li, G.; Watanabe, K.; Taniguchi, T.; Andrei, E. Y. MoS2: Choice Substrate for Accessing and Tuning the Electronic Properties of Graphene. *Phys. Rev. Lett.* **2014**, *113*, 156804.
(68) Ebnonnasir, A.; Narayanan, B.; Kodambaka, S.; Ciobanu, C. V. Tunable MoS2 bandgap in MoS2-graphene heterostructures. *Appl. Phys. Lett.* **2014**, *105*, 031603.
(69) Du, X. Z.; Uddin, M. R.; Li, J.; Lin, J. Y.; Jiang, H. X. Layer Number Dependent Optical Properties of Multilayer Hexagonal BN Epilayers. *Appl. Phys. Lett.* **2017**, *110*, 092102.
(70) Sponza, L.; Amara, H.; Attaccalite, C.; Latil, S.; Galvani, T.; Paleari, F.; Wirtz, L.; Ducastelle, F. Direct and Indirect Excitons in Boron Nitride Polymorphs: A Story of Atomic Configuration and Electronic Correlation. *Phys. Rev. B* **2018**, *98*, 125206.
(71) Ferreira, F.; Chaves, A. J.; Peres, N. M. R.; Ribeiro, R. M. Excitons in Hexagonal Boron Nitride Single-Layer: A New Platform for Polaritonics in the Ultraviolet. *J. Opt. Soc. Am. B* **2019**, *36*, 674−683.
(72) Geim, A.; Novoselov, K. The Rise of Graphene. *Nat. Mater.* **2007**, *6*, 183−191.
(73) Najmaei, S.; Liu, Z.; Zhou, W.; Zou, X.; Shi, G.; Lei, S.; Yakobson, B. I.; Idrobo, J. C.; Ajayan, P. M.; Lou, J. Vapour Phase Growth and Grain Boundary Structure of Molybdenum Disulphide Atomic Layers. *Nat. Mater.* **2013**, *12*, 754−759.
(74) Li, X.; Cai, W.; An, J.; Kim, S.; Nah, J.; Yang, D.; Piner, R.; Velamakanni, A.; Jung, I.; Tutuc, E.; Banerjee, S. K.; Colombo, L.; Ruoff, R. S. Large-Area Synthesis of High-Quality and Uniform Graphene Films on Copper Foils. *Science* **2009**, *324*, 1312−1314.
(75) Kim, K. K.; Hsu, A.; Jia, X.; Kim, S. M.; Shi, Y.; Hofmann, M.; Nezich, D.; Rodriguez-Nieva, J. F.; Dresselhaus, M.; Palacios, T.; Kong, J. Synthesis of Monolayer Hexagonal Boron Nitride on Cu Foil Using Chemical Vapor Deposition. *Nano Lett.* **2012**, *12*, 161−166.
(76) Frisenda, R.; Navarro-Moratalla, E.; Gant, P.; Pérez De Lara, D.; Jarillo-Herrero, P.; Gorbachev, R. V.; Castellanos-Gomez, A. Recent Progress in the Assembly of Nanodevices and Van Der Waals Heterostructures by Deterministic Placement of 2D Materials. *Chem. Soc. Rev.* **2018**, *47*, 53−68.

https://doi.org/10.1021/acsami.2c20100
ACS Appl. Mater. Interfaces 2023, 15, 2468−2478